EES Solar

PAPER

View Article Online
View Journal | View Issue

Cite this: *EES Sol.*, 2025, **1**, 1148

In situ 2D-perovskite-like ligands offer versatile passivation of large and small sized PbS quantum dots for infrared photovoltaics

Kai Liao,†[a] Beining Dong,†[b] Yajie Yan,[a] Xiaoxiao Zhang,[a] Kou Li,[b] Dewei Chu,[b] Long Hu *[b] and Ziqi Liang *[a]

Solution-processed lead sulfide (PbS) colloidal quantum dots (CQDs) have emerged as promising optoelectronic materials due to their size-tunable optical bandgaps and multiple exciton generation. Short-chain lead iodide and halide perovskites demonstrated effective passivation of polar <111> facets with Pb atom-only termination. Yet they failed to sufficiently passivate non-polar <100> facets that exhibit S/Pb dual-terminations—prevalent in larger-sized CQDs. Moreover, their weak ionic nature renders them vulnerable to moisture and oxygen exposure. Here we introduce a robust 2D neat perovskite $(BA)_2PbI_4$ for surface engineering of PbS CQDs *via* an *in situ* solution-phase ligand-exchange strategy. Such treatment forms a thin shell of BA^+ and I^- ions on the CQD surface, especially on the challenging non-polar <100> facets, enabling strong inward coordination that effectively reduces surface defect density and prevents CQD aggregation and fusion. Infrared solar cells employing $(BA)_2PbI_4$-capped large-sized PbS CQDs (1.0 eV-bandgap) as active layers achieved an impressive power conversion efficiency (PCE) of 8.65% coupled with excellent ambient stability, attributed to the hydrophobic nature of the BA^+-rich surface. The same ligand strategy also proved versatile for small-sized PbS CQDs (1.3 eV), yielding a champion PCE of 13.1% and significantly enhanced thermal stability in devices compared to the control device of PbI_2-capped analogues (11.3%).

Received 20th August 2025
Accepted 8th October 2025

DOI: 10.1039/d5el00135h

rsc.li/EESSolar

Broader context

Since infrared photons account for nearly 55% of the solar spectrum, infrared photovoltaics capable of harvesting this energy have attracted significant interest. Conventional halide perovskite and silicon devices are limited in this range, whereas PbS colloidal quantum dots (CQDs), with a large Bohr exciton radius (~20 nm), offer wide bandgap tunability (0.6–1.5 eV) through size control, making them promising candidates for infrared optoelectronics. However, existing passivation strategies cannot universally address surface defects, as dominant crystalline facets shift from (111) to (100) with increasing CQD size. This causes poor colloidal stability, high defect density, and degraded photo-thermal stability, ultimately limiting device performance. Here, we report a robust 2D perovskite-like ligand, $(BA)_2PbI_4$, for surface engineering of PbS CQDs *via* an *in situ* solution-phase ligand-exchange process. A thin shell of BA^+ and I^- ions forms on the CQD surface, stabilizing non-polar <100> facets, reducing defects, and preventing aggregation. Infrared photovoltaics incorporating $(BA)_2PbI_4$-capped PbS CQDs with a 1.0 eV bandgap achieved a power conversion efficiency (PCE) of 8.65% and excellent ambient stability due to the hydrophobic BA^+ surface. Furthermore, large-bandgap PbS CQDs (1.3 eV) treated with the same ligand delivered a champion PCE of 13.1% with superior thermal stability compared to PbI_2-capped controls (11.3%).

1. Introduction

Lead sulfide (PbS) colloidal quantum dots (CQDs) exhibit peculiar optical properties for optoelectronic devices including their near-infrared (NIR) absorption, high absorption coefficients and tunable optical bandgaps *via* size control and solution processability.[1–7] Of particular interest is that single-junction CQD solar cells (CQDSCs) hold great potential to go beyond the Shockley–Queisser limit thanks to the presence of multiple exciton generation (MEG) within PbS CQDs.[8–11] Recent advances by virtue of synthesis optimization,[12,13] ligand modification,[14–16] and interface engineering[17–19] have now elevated the PbS CQDSCs up to a record power conversion efficiency (PCE) of over 15%.[20]

Organic–inorganic metal halide perovskites have recently emerged and exhibited superior defect tolerance and high carrier mobilities.[21–23] Benefiting from ligand and matrix engineering, a plausible integration of PbS CQDs and halide perovskite semiconductors into a single device can enable full utilization of their intriguing merits such as NIR light

[a]*Department of Materials Science, Fudan University, Shanghai 200433, China. E-mail: zqliang@fudan.edu.cn*

[b]*School of Materials Science and Engineering, University of New South Wales (UNSW), Sydney, NSW 2052, Australia. E-mail: long.hu@unsw.edu.au*

† K. Liao and B. Dong equally contributed to this work.

absorption of PbS CQDs and high defect tolerance of perovskites, which led to higher short-circuit current density (J_{SC}) and open-circuit voltage (V_{OC}), respectively, in hybrid CQDSCs.[24–27] For instance, Sargent and coworkers demonstrated the growth of $MAPbI_3$ perovskite ligands on PbS CQDs by using solution-phase ligand-exchange followed by spin-coating and thermal annealing to form a perovskite matrix, realizing more efficient defect passivation and an excellent PCE of 8.95%.[28] Alternately, we employed a solid-state ligand-exchange strategy to obtain $MAPbI_3$-capped PbS and solution phase PbI_2-KI complex capped PbS CQDs, giving rise to PCEs of 5.28% [29] and 12.1%,[30] respectively. Thus far, various three-dimensional (3D) halide perovskite ligands such as $CsPbX_3$ and $GuPbX_3$ have been reported to be successfully introduced onto PbS CQDs, boosting the PCEs up to 13.80%.[31–36]

Distinct from 3D analogues, on the other hand, two-dimensional (2D) halide perovskites possess layered structures and display enhanced ambient stability as a result of the hydrophobicity and the inhibition of ion migration provided by long-chain spacers in-between perovskite octahedra.[37] In light of these unique merits, it would be worthwhile to graft 2D perovskites onto PbS CQDs. To exemplify this, Sargent and coworkers demonstrated a matrix engineering strategy to form a self-confined 2D layered structure, which acted to suppress the inhomogeneity of the matrix and thus adjusted inter-nanoparticle spacings on the atomic scale, leading to a reduction in structural and energetic disorder and hence a certified record PCE of 12%.[38] Most recently, Vaynzof *et al.* exploited a simple approach to spacer cation-mediated removal of excess inter-dot lead halides, resulting in better charge transportation and an excellent PCE of 11.80%.[39] Furthermore, excellent durability and an ultrafast excitonic energy transfer were obtained by incorporating PbS CQDs into the low-dimensional perovskite matrix for the applications of LEDs and PDs.[40,41] These research studies were however mostly centered on matrix engineering to embed 2D perovskites into PbS CQDs by solvent or antisolvent post-treatments. The interaction and mechanisms, such as *in situ* ligand engineering between PbS CQDs and 2D perovskite precursors, which will significantly affect the device performance and stability, remain to be fully clarified. Besides, most studies focused upon phenylethylamine (PEA) and its derivatives as spacer cations for LEDs or PDs rather than CQDSCs. Of critical importance, the inherent colloidal and device stabilities of CQDs remain highly challenging for practical applications.

This study presents a facile *in situ* solution-phase ligand-exchange method towards the formation of 2D-perovskite-like $(BA)_2PbI_4$ ligands on PbS CQDs for efficient and stable photovoltaic devices. In comparison to conventional PbI_2 and $MAPbI_3$ ligands, the $(BA)_2PbI_4$ capping ligands formed a robust shell of BA^+ and I^- rather than a perovskite matrix on the surface of CQDs, which particularly enabled strong inward coordination with the nonpolar <100> facet, resulting in excellent photo- and thermal-stabilities. In addition, the versatility of efficient surface passivation for both large- and small-bandgap PbS CQDs as active layers was demonstrated, which achieved impressive PCEs of 8.65% (1.0 eV) and 13.1% (1.3 eV) in solar cells, respectively. This versatile 2D perovskite-like ligand approach holds promise for broader applications to other quantum dot systems, offering reduced defect densities, elevated device efficiencies, and enhanced colloidal and environmental stabilities.

2. Results and discussion

The benchmark oleic acid (OA)-capped PbS (denoted as PbS-OA) CQDs were synthesized *via* the hot-injection method by following the literature,[7] followed *via* solution-phase ligand-exchange of OA with $(BA)_2PbI_4$ ligands. Two batches of PbS CQDs are synthesized in this work including small- and large-sized CQDs with corresponding exciton peaks at 933 nm (~1.3 eV-bandgap) and 1180 nm (~1.0 eV-bandgap). Large-sized CQDs have more non-polar <100> planar facets with dual termination of S and Pb atoms, resulting in reduced surface passivation efficiency and worse colloidal/photo-thermal stabilities in comparison to small-sized CQDs with <111> dominated facets with only Pb atom termination. Therefore, large-sized PbS CQDs (1.0 eV) will be employed in this study for a thorough investigation to examine the efficacy of surface passivation without further clarification. Additionally, small-sized CQDs (1.3 eV) will serve as hole-transport layers in large-sized CQD-based active layer solar cells due to better band-alignment. Moreover, since the 1.3 eV of PbS CQDs is optimal for single-junction cells, small-sized PbS CQDs as active layers will also be used to construct high-performing solar cells to examine the surface passivation versatility of 2D perovskite-like ligands developed in this work.

In the first step, a stoichiometric mixture of PbI_2, *n*-BAI and ammonium acetate was dispersed in DMF solvent and subsequently used as the 2D perovskite precursor and injected into the PbS-OA CQD solution. Note that ammonium acetate was applied to assist colloidal stabilization during ligand exchange. In the second, by mixing the PbS-OA CQD solution in nonpolar *n*-octane solvent with the precursor solution of *n*-BAI and PbI_2 in polar DMF solvent, neat 2D-perovskite-like $(BA)_2PbI_4$ ligands were formed on PbS CQDs by displacing the native long-chain OA ligands. Consequently, PbS CQDs were dispersed in polar DMF solvent and this phase-transfer process indicates the incorporation of $(BA)_2PbI_4$ ligands on PbS CQDs, yielding PbS-$(BA)_2PbI_4$ CQDs and hence confirming the success of ligand exchange.

In principle, nonpolar toluene solvent was used to precipitate CQDs and remove impurities as anti-solvent during post-step purification. However, the introduction of the anti-solvent compromises structural stability of CQDs and impaired the performance of photoelectric devices.[42] In this respect, we compared the stability of PbS CQD solution capped by PbI_2, $MAPbI_3$ and $(BA)_2PbI_4$ ligands, respectively. It is noticed that both PbS-PbI_2 and PbS-$MAPbI_3$ CQD solutions change in color from black to gray after gradually increasing the amount of toluene solvent as shown in Fig. S1a (SI), indicating severe aggregation of CQDs.[43] In contrast, the color of PbS-$(BA)_2PbI_4$ CQD solution remains blackish even after adding an excessive toluene, suggestive of its excellent colloidal stability during

purification. Subsequently, centrifugal precipitation was conducted to further check whether the precipitated CQD solids were agglomerated.

As shown in Fig. 1a, PbS-$MAPbI_3$ and the PbS-PbI_2 CQD powders appeared to be obviously grayish, in stark contrast to the preserved stably blackish PbS-$(BA)_2PbI_4$ CQDs. To explain this phenomenon, a schematic diagram is proposed as illustrated in Fig. 1b wherein the capping ligands of PbS-$MAPbI_3$ and PbS-PbI_2 CQDs tend to interact with the antisolvent molecules and detach from their surface after adding excessive toluene, resulting in severe aggregation of CQDs. In contrast, the BA^+ ligands of PbS-$(BA)_2PbI_4$ CQDs have stronger inward coordination with the sulfur atoms on nonpolar <100> facets, thereby preventing their detachment from the surface of CQDs. In parallel, we also compared the colloidal stability of these CQDs with the same concentration in BA solvent as shown in Fig. S1b (SI). It can be seen that the PbS-$(BA)_2PbI_4$ CQD solution remains blackish after filtering twice in comparison to PbS-$MAPbI_3$ and PbS-PbI_2 CQD solutions, indicating that most of the PbS-$(BA)_2PbI_4$ CQDs are not agglomerated but colloidally

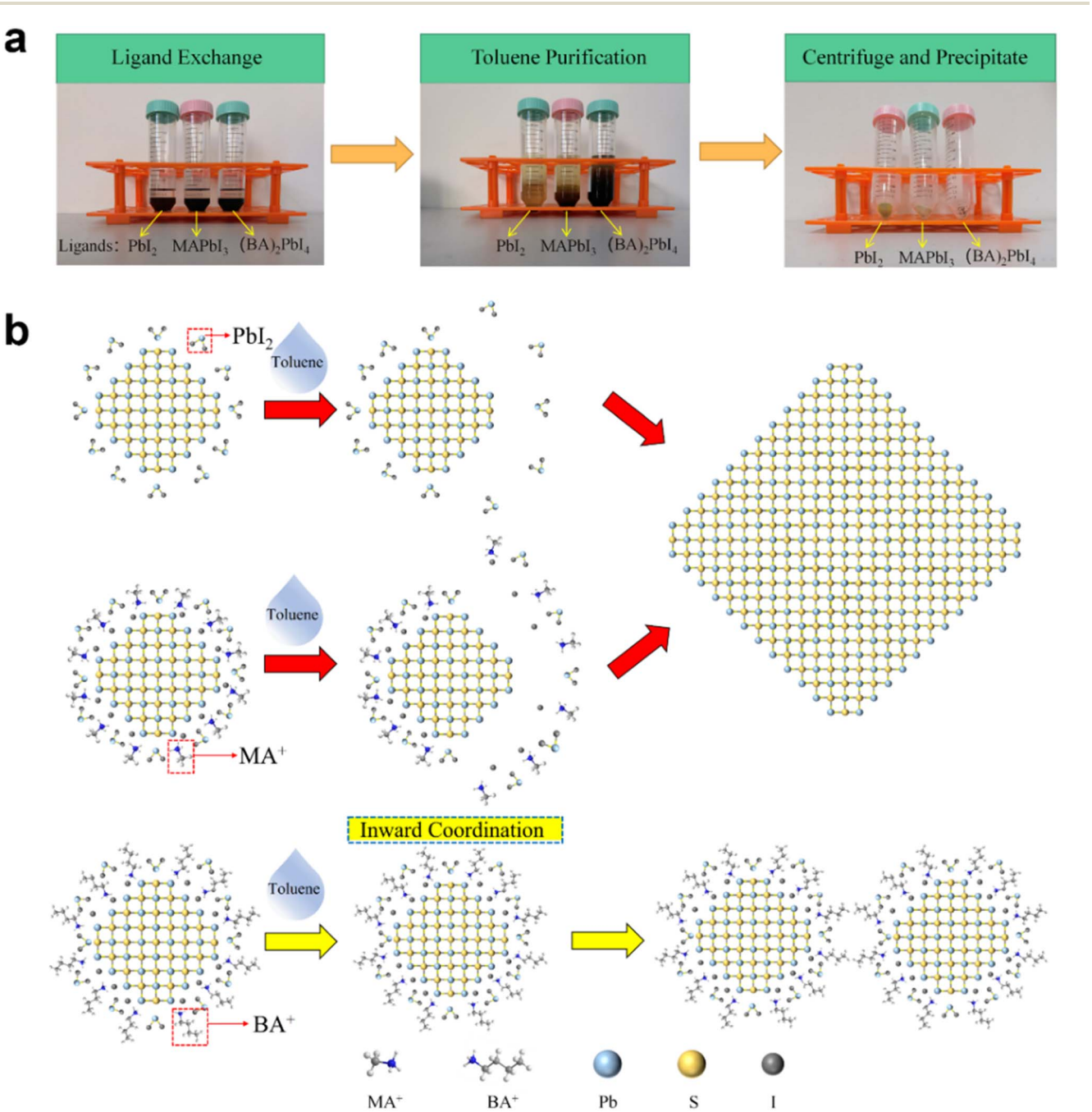

Fig. 1 (a) Colloidal stability comparison of CQD solution after ligand exchange, toluene purification and centrifugal precipitation, respectively. (b) Schematic illustration of the changes of the PbS CQD surface with different ligands after toluene purification.

stable in solution. The outstanding colloidal stability of PbS-$(BA)_2PbI_4$ CQD solution is largely attributed to the relatively long-chain BA^+ ligands, increasing the distance between adjacent CQDs and preventing them from aggregation.

To verify the above argument, we performed density functional theory (DFT) calculations on the adsorption energy (E_{ad}) of I^- (in PbI_2, $MAPbI_3$ and $(BA)_2PbI_4$), MA^+ (in $MAPbI_3$), and BA^+ (in $(BA)_2PbI_4$) ligands to CQDs as shown in Fig. S2 (SI). Note that the lead-rich polar <111> facets of PbS CQDs bound preferentially to I^- due to strong electrostatic interactions,[44] while the nonpolar <100> facets could not efficiently be passivated by halide anions due to electro-neutral facets, which are therefore chosen for calculations to highlight the impacts of MA^+ and BA^+ ligands. It is found that the E_{ad} values of I^- and MA^+ are −2.03 and −2.14 eV to <100> facets, respectively, whereas BA^+ has a higher E_{ad} of −2.49 eV, indicating its stronger binding to the surface of PbS CQDs, particularly to (100) facets. In addition, Fig. S3 (SI) compares the S 2p and N 1s XPS spectra and the detection of nitrogen atoms in PbS-$(BA)_2PbI_4$ powder confirms the successful ligand-exchange of BA^+. Furthermore, the binding energy (E_B) value of the S 2p species of PbS-$(BA)_2PbI_4$ is estimated to be *ca.* 0.23 eV lower than that of PbS-PbI_2, which is ascribed to the interactions between BA^+ ligands and the sulfur atoms on the surface. Our studies confirm that $(BA)_2PbI_4$ ligands are less inclined to detach from CQD surfaces than PbI_2 and $MAPbI_3$.[45]

Since $MAPbI_3$ and PbI_2 capped PbS CQDs were previously well-characterized,[46,47] here only $(BA)_2PbI_4$ and pristine OA-capped PbS CQDs with bandgaps of 1.3 eV were thoroughly characterized for comparison in the following parts. First, transmission electron microscopy (TEM) was employed to visualize the ligand-exchange process of PbS CQDs. As shown in Fig. 2a, a slight decrease in the average size is found in PbS-$(BA)_2PbI_4$ CQDs after ligand-exchange, that is, 3.7 ± 0.5 nm in comparison to neat PbS-OA CQDs (4.1 ± 0.5 nm). The size reduction can be presumably ascribed to the dissociation of surface atoms benefiting from the interaction between CQDs and the solvent during ligand-exchange, suggesting strong interactions. Fig. 2b compares the ultra-violet-visible-infrared (UV-Vis-IR) absorption and photoluminescence (PL) spectra of PbS-OA CQDs in *n*-hexane and PbS-$(BA)_2PbI_4$ CQDs in *n*-butylamine solution, respectively. It can be seen that the first excitonic absorption peak of PbS-OA CQDs is located at 1180 nm, which is consistent with the corresponding sizes (4.1 nm seen from Fig. 2a) of PbS-OA CQDs, according to the empirical formula (1):[48]

$$E_0 = 0.41 + \frac{1}{0.0252d^2 + 0.283d} \quad (1)$$

where E_0 is the optical bandgap extracted from the absorption spectra *via* the Tauc plot method as shown in Fig. S4a (SI) and d is the particle size of PbS CQDs. Notably, the calculated E_0s

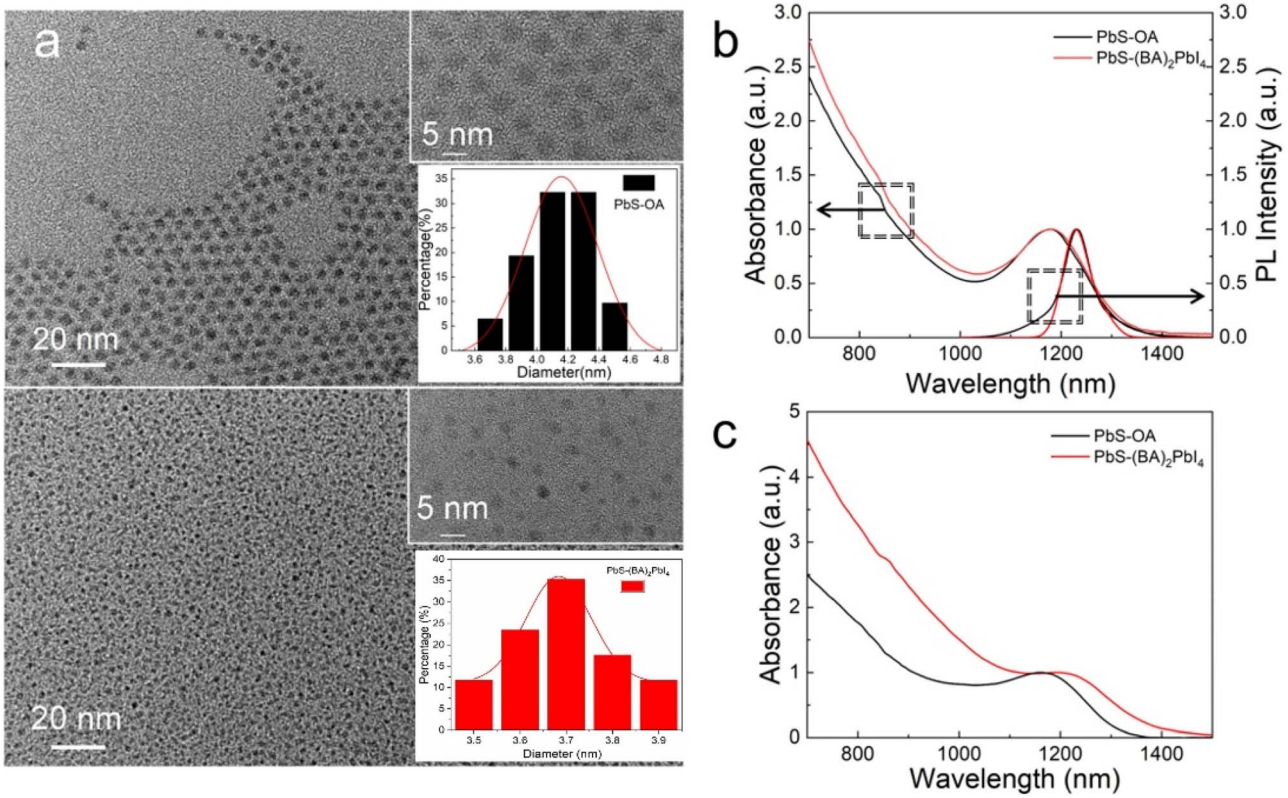

Fig. 2 (a) TEM images of PbS CQDs prior to and after the ligand-exchange process with an inset illustrating the particle size distribution. (b) UV-vis absorption and PL spectra comparison of PbS-OA CQDs in *n*-hexane and PbS-$(BA)_2PbI_4$ CQDs in *n*-butylamine solution. (c) Comparative UV-vis absorption spectra of PbS CQD films.

values are 0.96 and 0.97 eV for PbS-$(BA)_2PbI_4$ and PbS-PbI_2 films, respectively, which are slightly smaller than 1.0 eV. In addition, the first excitonic peak of the PbS-$(BA)_2PbI_4$ CQDs shows a slight red-shift of 3 nm after ligand-exchange processes as seen in Fig. 2a. As such, a 1 nm red-shift is seen in the PL spectrum of PbS-$(BA)_2PbI_4$ CQDs relative to PbS-OA CQDs with the FWHM of the former being slightly narrower (65 nm) than that of the latter (66 nm), which is presumably attributed to uniform size distribution and less QD aggregation, likely resulting from better surface passivation as investigated in detail in the following section. Fig. 2c compares the UV-vis absorption spectra of PbS-OA and PbS-$(BA)_2PbI_4$ CQDs thin films. Relative to the PbS-OA CQDs film, the exciton peak of the CQDs passivated with $(BA)_2PbI_4$ ligands shows a large red-shift of 25 nm due to the significantly enhanced electron coupling after insulating OA removal,[49] in accord with the results of optical properties in solution.

To confirm the removal of OA and the presence of $(BA)_2PbI_4$ ligands on the PbS CQD surface, Fourier transform infrared (FT-IR) measurements were performed on PbS-$(BA)_2PbI_4$ powder as shown in Fig. 3a. The characteristic vibrations of *n*-BA are found in PbS-$(BA)_2PbI_4$, in which the N–H stretch from BA^+ is located at 3300–3000 cm^{-1} and the peaks of 3000–2800 cm^{-1} and 1530 cm^{-1} corresponded to the C–H and C═O stretch modes

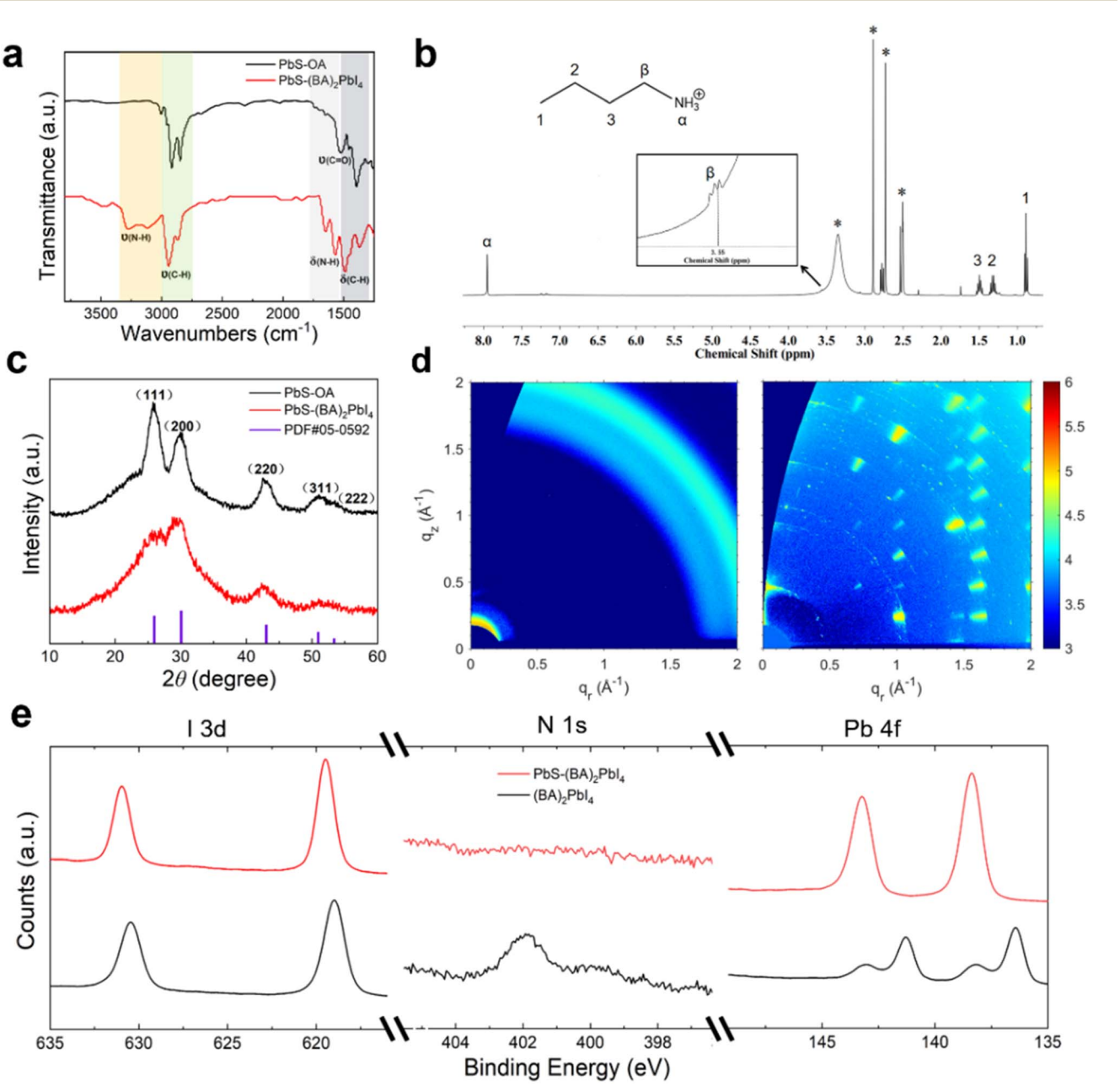

Fig. 3 (a) FTIR spectra of PbS CQDs before and after ligand-exchange. (b) ^1H NMR spectrum of PbS-$(BA)_2PbI_4$. (c) XRD patterns of PbS-OA and PbS-$(BA)_2PbI_4$ films. (d) GIWAXS patterns of neat $(BA)_2PbI_4$ and PbS-$(BA)_2PbI_4$ CQDs thin films. (e) XPS profiles of $(BA)_2PbI_4$ (black line) and PbS-$(BA)_2PbI_4$ (red line) films, showing I 3d, Pb 4f, and N 1s bands.

from OA^-, respectively, whereas the scissor modes of N–H and C–H are located between 1750–1550 and 1520–1400 cm^{-1}, respectively. It is noticed that the intensities of C–H and C=O peaks remarkably decrease after ligand-exchange as shown in Fig. S4b (SI), suggesting that most of the OA ligands are replaced by $(BA)_2PbI_4$ ligands.

Moreover, we acquired the ^{1}H-NMR spectrum on PbS-$(BA)_2PbI_4$ powder in C_2D_6SO solvent as shown in Fig. 3b to further verify whether the $(BA)_2PbI_4$ ligands have been successfully exchanged onto PbS CQDs. It can be seen that several resonances related to protons of the alkyl region (peaks identified from 1–3) are located at 0.88, 1.30 and 1.49 ppm, respectively, with pronounced multiple peaks. The chemical shifts at 7.95 and 3.50 ppm are assigned to the ammonium species with the α peak to the R-NH_3^+ proton and the β resonance arising from the α-CH_2 protons, respectively. We also noted that there is almost no signal peak associated with the sp^2 alkene protons of the OA ligand in 5–6 ppm, in good agreement with the FTIR results. Besides, the asterisk marked peaks are identified to arise from the C_2D_6OS and residual DMF solvents.

We then compared the crystal structures of thin films of PbS CQDs capped by OA and $(BA)_2PbI_4$ ligands, as shown in Fig. 3c. The XRD profiles of PbS-OA and PbS-$(BA)_2PbI_4$ are almost identical, in good agreement with the standard card of PbS, suggesting that the diffraction patterns of ligand-exchanged PbS CQDs are dominated by strong PbS signals. Grazing-incidence wide-angle X-ray scattering (GIWAXS) patterns are shown in Fig. 3d, where the neat $(BA)_2PbI_4$ film displayed layered features such as sharp and discrete Bragg spots along the q_z axis (*i.e.*, $q_z = 0$ direction at 0.5 $Å^{-1}$), whereas the PbS-$(BA)_2PbI_4$ film presented the characteristic signals of PbS CQDs. Therefore, we posit that the $(BA)_2PbI_4$ ligands are formed as an ultra-thin shell structure on PbS CQDs rather than a 2D perovskite matrix after spin-coating and post-annealing of thin films. This would enhance colloidal stability and not affect charge transportation properties in the device, which will be discussed later.

To gain an insight into the fine structures of PbS CQDs films, X-ray photoelectron spectroscopy (XPS) characterization was conducted on the $(BA)_2PbI_4$ and PbS-$(BA)_2PbI_4$ films. Fig. 3e compares the I 3d, N 1s and Pb 4f XPS spectra. It is found that the E_B values of the I $3d_{5/2}$ and Pb $4f_{7/2}$ species of PbS-$(BA)_2PbI_4$ are *ca.* 0.8 and 1.2 eV higher than that of $(BA)_2PbI_4$, respectively, which is ascribed to the strong coordination between CQDs and

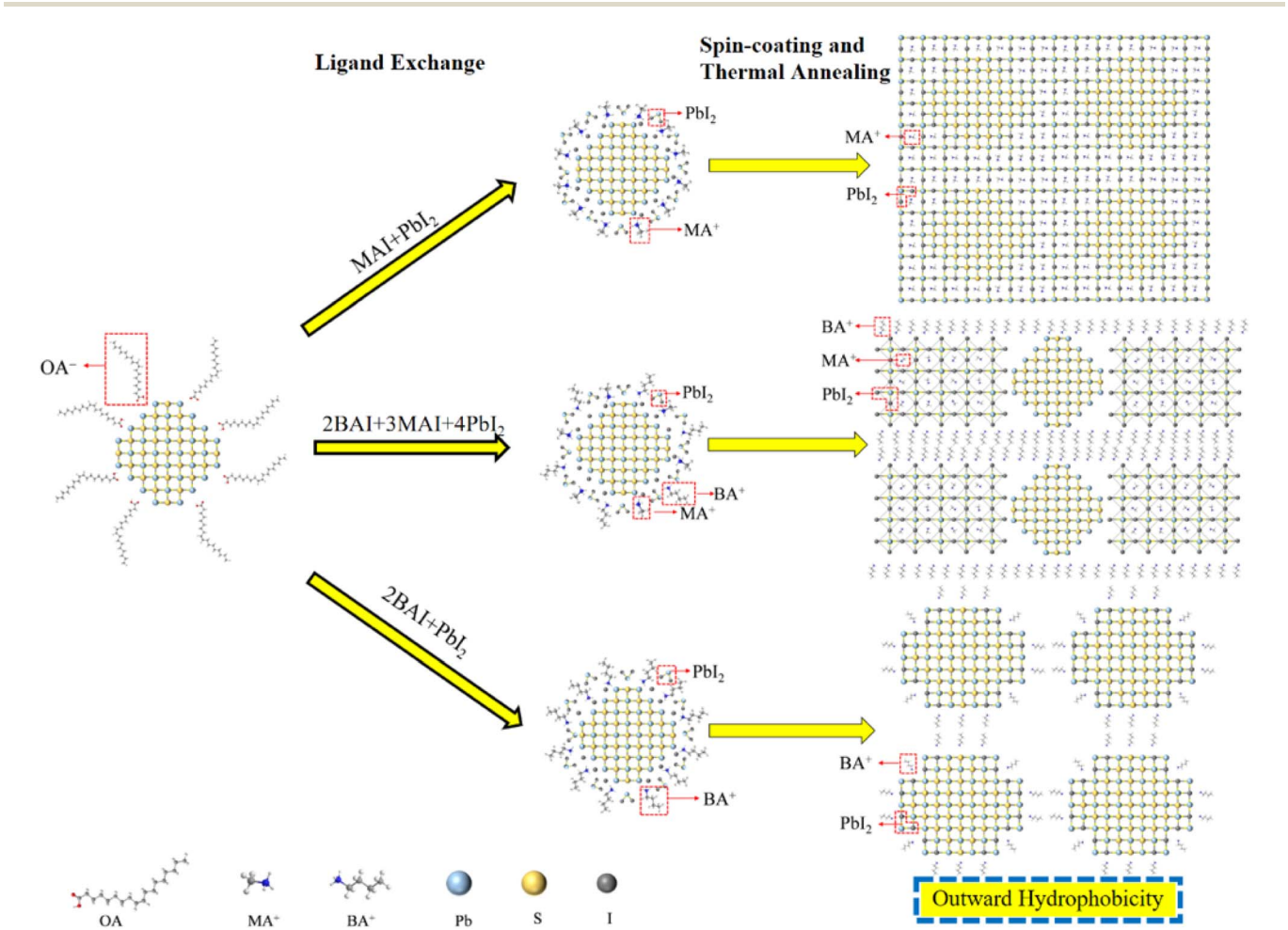

Fig. 4 Illustration of film-forming processes of PbS-$MAPbI_3$, PbS-$(BA)_2(MA)_4Pb_5I_{16}$, and PbS-$(BA)_2PbI_4$ *via* a sequence of ligand-exchange and spin-coating followed by thermal annealing.

2D perovskite ligands, further confirming the absence of a 2D perovskite matrix in PbS-$(BA)_2PbI_4$ CQD films.

Herein, a tentative scheme is proposed to illustrate the process of ligand-exchange and film fabrication of PbS CQDs with different perovskites. As schematically shown in Fig. 4, $MAPbI_3$ ligands act to form perovskite bridges between the adjacent PbS CQDs, benefiting from excellent lattice match as previously reported.[19] The same mechanism is also applicable to other 3D perovskites such as $CsPbI_3$ and $FAPbI_3$. As for quasi-2D perovskite, for instance, $(BA)_2(MA)_{n-1}Pb_nI_{3n-1}$, it can be seen that only when the perovskite vertical dimensional <n> value is high enough to be above 5 can the perovskite crystals and organic cations match well with PbS CQDs.[39] Besides, another challenge for quasi-2D perovskite ligands is that the quasi-2D perovskite precursor solution of a precise molar ratio used for ligand exchange cannot ensure the formation of perovskite with the desired n value, which is likely to be solved by pure 2D perovskite precursor solution of $n = 1$. However, previous literature reports speculated the absence of 2D perovskites that can be ascribed to the fact that the pure 2D perovskite layer is too thin to incorporate into PbS CQDs.[39] Based on the above arguments, we believe that the $(BA)_2PbI_4$ ligands functioned as a mixture of BA^+ and I^- ultra-thin shells to passivate surface defects of PbS CQDs rather than as a perovskite matrix after forming thin films, which is well consistent with the GIWAXS results.

Both PbS-$(BA)_2PbI_4$ and PbS-PbI_2 films with bandgaps of 1.0 eV were thoroughly characterized to evaluate their suitability for solar cell fabrication. The surface morphology of both active layers was first examined by using tapping-mode atomic force microscopy (TP-AFM), as shown in Fig. 5a. Both PbS-$(BA)_2PbI_4$ and PbS-PbI_2 films exhibit comparable root-mean-square (RMS) roughness values of 14.4 Å and 15.7 Å, respectively. However, the PbS-$(BA)_2PbI_4$ films display fewer surface voids, likely due to the uniform colloidal solution. Time-resolved photoluminescence (TRPL) decay measurements, as shown in Fig. 5b,

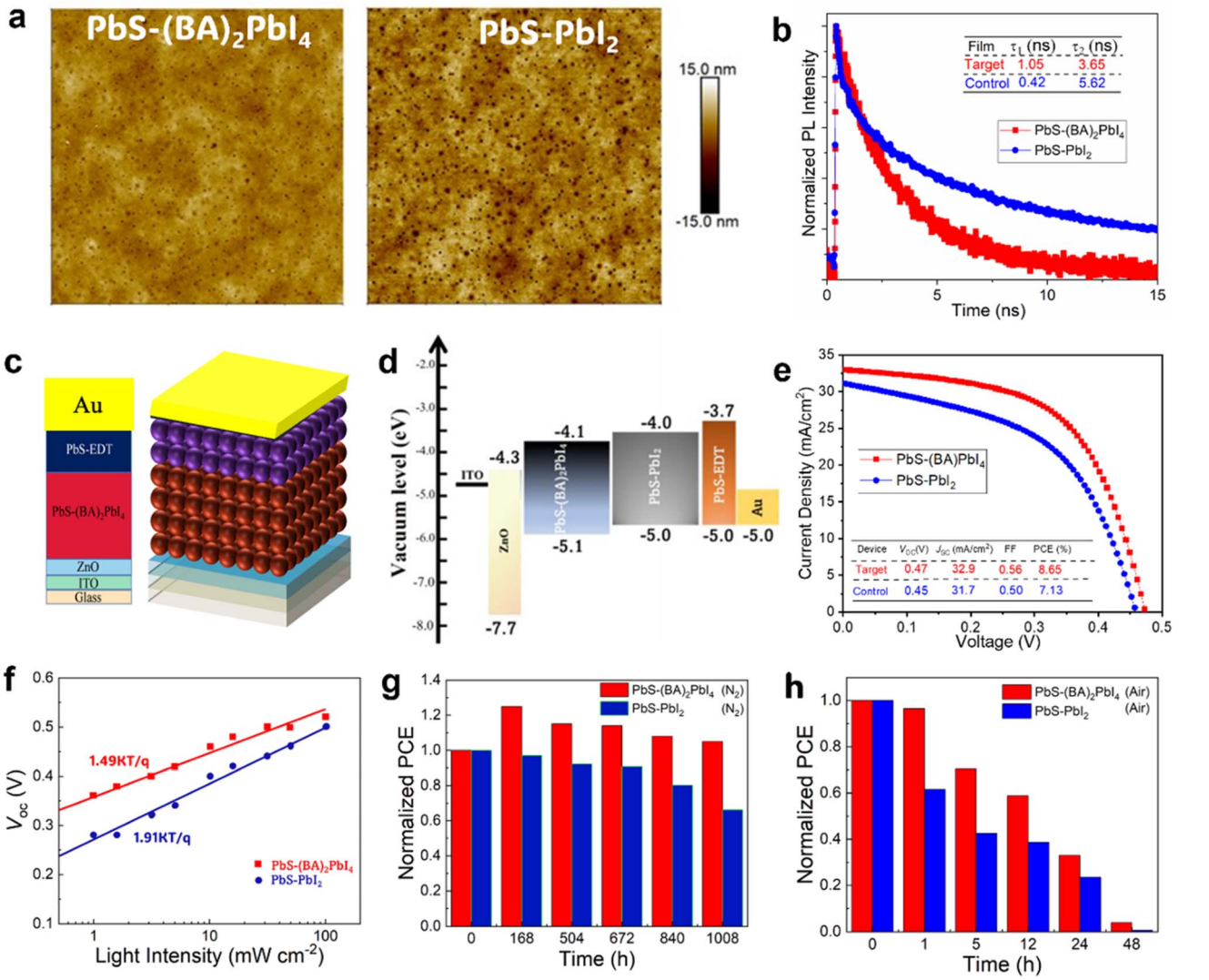

Fig. 5 Comparison of PbS-$(BA)_2PbI_4$ and PbS-PbI_2 CQD films and devices. (a) TP-AFM images and (b) TRPL spectra. (c) Schematic of CQD solar cells with (d) energy band structures, and (e) J–V curves. (f) Light intensity dependences of V_{OC} for CQD devices. Lifetime curves of CQD devices after storage in (g) Ar and (h) air (80–90% RH) atmospheres.

further reveal improved carrier dynamic properties in the PbS-$(BA)_2PbI_4$ films. Specifically, the carrier lifetime associated with trap-assisted non-radiative recombination (τ_1) in PbS-$(BA)_2PbI_4$ is significantly longer (1.05 μs *vs.* 0.42 μs), while the lifetime associated with carrier transfer (τ_2) is shorter (3.56 μs *vs.* 5.62 μs), compared to the PbS-PbI_2 control film. These results suggest reduced trap state density and enhanced charge transfer dynamics in the PbS-$(BA)_2PbI_4$ films.

Finally, CQD solar cells were fabricated using a device architecture of ITO/ZnO/1.0 eV-PbS CQDs/1.3 eV-PbS-EDT/Au, incorporating a sol–gel prepared ZnO electron-transport layer (ETL) and a spin-coated hole-transport layer (HTL) composed of 1,2-ethanedithiol (EDT)-treated 1.3 eV-PbS CQDs, as shown in Fig. 5c. Cross-sectional SEM of a whole device shows that the thickness of the PbS PbS-$(BA)_2PBI_4$ active layer is 370 nm as shown in Fig. S5a. Ultraviolet photoelectron spectroscopy (UPS) measurements were conducted to determine the energy levels of the PbS-$(BA)_2PbI_4$ layer and the control PbS-PbI_2 CQDs. The Fermi levels (E_{Fs}) were found to be −4.5 eV for the PbS-$(BA)_2PbI_4$ film and −4.6 eV for the PbS-PbI_2 film (see Fig. S5b and c in the SI). The valence band energies were calculated by adding the onset energy (E_{onset}) to the E_F values while the conduction band energies were determined by combining the bandgap of PbS CQDs. The band energy positions of ZnO and 1.3 eV-PbS-EDT films were obtained from the values from ref. 50 and 51. As shown in Fig. 5d, both films exhibit favorable band alignment at the CQD/ETL and CQD/HTL interfaces, ruling out band alignment as a limiting factor for device performance. The current density–voltage (*J*–*V*) characteristics under AM1.5G illumination at 100 mW cm^{-2} are presented in Fig. 5e. The control devices based on PbS-PbI_2 CQDs exhibit a PCE of 7.13%, with V_{OC} = 0.45 V, J_{SC} = 31.7 mA cm^{-2}, and a fill factor (FF) of 50%. In comparison, the device based on PbS-$(BA)_2PbI_4$ CQDs achieves a significantly higher PCE of 8.65%, with V_{OC} = 0.47 V, J_{SC} = 32.9 mA cm^{-2}, and a notably improved FF of 58%. Note that the champion PCE of 8.65% obtained in this study—using 1.0 eV-PbS CQDs—ranks among the highest efficiencies reported to date for CQD solar cells within this bandgap.[52]

To gain an insight into the charge recombination mechanisms, we examined the light-intensity dependence of V_{OC}. As shown in Fig. 5f, deviations in the slope from the ideal value $k = KT/q$ (where K is the Boltzmann constant, T is absolute temperature, and q is the elementary charge) indicate trap-assisted recombination in photovoltaic devices. The diode ideality factors (k) are calculated to be 1.49 for the PbS-$(BA)_2PbI_4$ devices and 1.91 for the PbS-PbI_2 devices. The lower k value in the former confirms reduced trap-assisted recombination, indicating more effective defect passivation by the $(BA)_2PbI_4$ ligands.

We then assessed the operational stability of the devices stored in an Ar atmosphere, with measurements conducted under AM1.5G illumination in air (Fig. 5g and h). Remarkably, the PCE of the PbS-$(BA)_2PbI_4$ devices raises up to ~125% of the initial value after 168 hours and then stabilizes to around 105% after 1000 hours. In contrast, the PCE of the PbS-PbI_2 devices declines steadily to ~65% over the same period. Previous studies have attributed such recovery effects to p-doping of the EDT-treated layer by oxygen and moisture.[35] However, oxygen

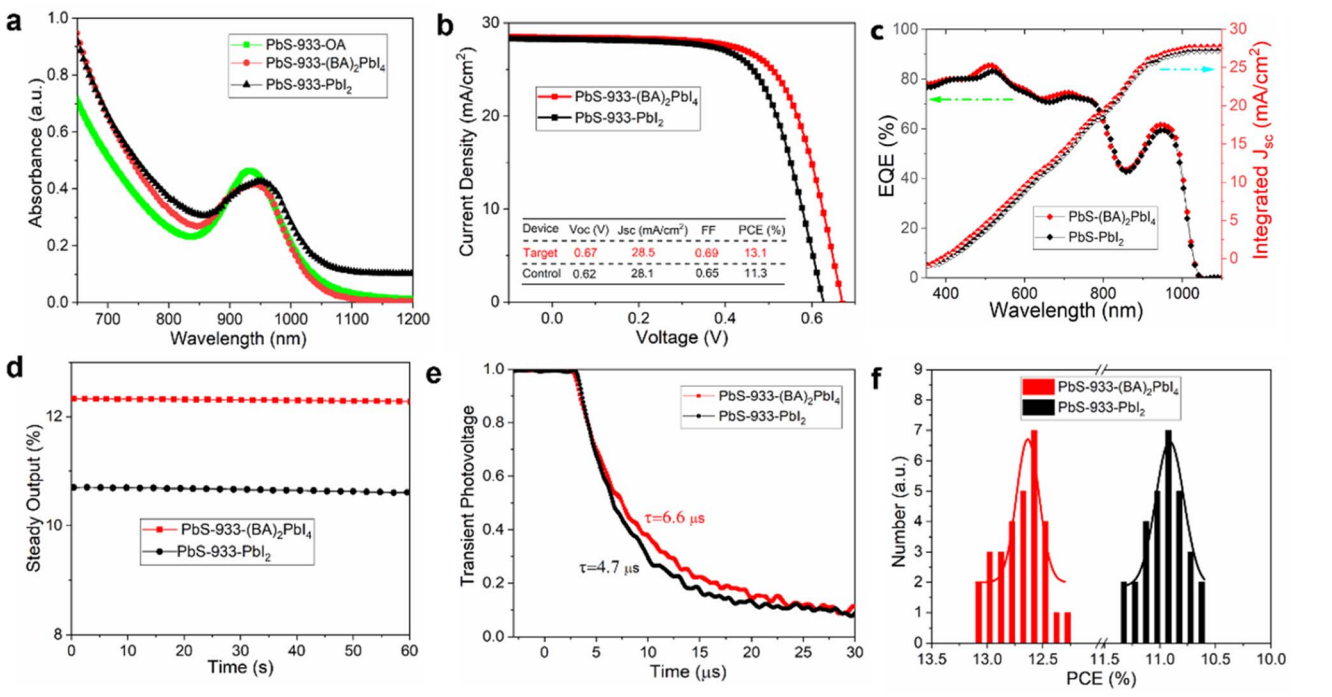

Fig. 6 (a) UV-Vis-IR light absorption spectra of PbS-933-OA in solution and PbS-933-$(BA)_2PbI_4$ and PbS-933-PbI_2 in thin films. (b) *J*–*V* curves, (c) EQE spectra, (d) steady output of PCEs at maximum power points over 60 s, (e) transient photovoltage, and (f) PCE distribution of solar cells based on PbS-933-$(BA)_2PbI_4$ and PbS-933-PbI_2 films.

and water can also oxidize the CQD surface, leading to degradation.[36] These results further validate the robustness of this 2D perovskite-like ligand for surface passivation of CQDs.

We further investigated the surface passivation versatility of this 2D perovskite-like ligand $(BA)_2PbI_4$ for small-sized PbS CQDs (1.3 eV) used as active layers in solar cell applications. Fig. 6a presents the UV-Vis-IR light absorption spectra of OA-capped PbS CQDs with a first excitonic peak at 933 nm (denoted as PbS-933-OA) in hexane solution, as well as films capped with $(BA)_2PbI_4$ (*i.e.*, PbS-933-$(BA)_2PbI_4$) and PbI_2 (*i.e.*, PbS-933-PbI_2). Solar cell devices fabricated with identical architectures of ITO/ZnO/1.3 eV-PbS/1.3 eV-PbS-EDT/Au delivered a champion PCE of 13.1% for the PbS-933-$(BA)_2PbI_4$ film along with 11.3% for the PbS-933-PbI_2 film (Fig. 6b). The external quantum efficiency (EQE) spectra for both devices are shown in Fig. 6c. The PbS-933-$(BA)_2PbI_4$ device exhibits slightly higher EQE across the full spectral range (300–1000 nm), resulting in integrated current densities of 28.0 and 27.4 mA cm^{-2} for the target and control devices, respectively. In addition, steady output of PCEs of 12.5% and 10.7% at maximum power points remain unchanged over 60 seconds for the respective devices, indicating output stability (Fig. 6d).

Transient photovoltage (TPV) measurements show a longer carrier lifetime of 6.6 μs for the $(BA)_2PbI_4$-based device compared to 4.7 μs for the control (Fig. 6e), suggesting reduced carrier recombination. Furthermore, PCE distributions for 30 devices of each type (Fig. 6f) reveal average PCEs of 12.7% and 10.9% for the target and control devices, respectively. The statistics of V_{OC}, J_{SC} and FF for both types of solar cell of PbS-933-$(BA)_2PbI_4$ and PbS-933-PbI_2 are displayed in Fig. S6 (SI). Thermal stability was evaluated by tracking device performance with 15 devices for each type during continuous heating at 80 °C in air as shown in Fig. S7. After storage for 10 hours, the $(BA)_2PbI_4$-passivated device retains 89% of its initial average PCE, in contrast to the control one (only 67%) under the same conditions, which aligns with the results of large-sized CQDSCs. These results demonstrate that the 2D $(BA)_2PbI_4$ ligand provides effective surface passivation for both large- and small-sized PbS CQDs, enabling superior device performance, enhancing ambient tolerance and improving thermal stability.

3. Conclusion

In conclusion, we have demonstrated an effective and versatile strategy to simultaneously enhance both the performance and stability of PbS CQDSCs. The 2D perovskite-like ligand $(BA)_2PbI_4$ provides significantly stronger inward coordination with PbS CQDs compared to conventional ligands such as PbI_2, primarily through interactions between BA^+ and surface sulfur atoms on the PbS nanocrystals. Benefiting from enhanced defect passivation, solar cells employing $(BA)_2PbI_4$-capped PbS CQDs achieved PCEs of 8.65% and 13.1% using CQDs with optical bandgaps of 1.0 and 1.3 eV, respectively, significantly outperforming the control devices (7.13% and 11.3% under identical conditions). Notably, unencapsulated PbS-$(BA)_2PbI_4$ devices also exhibited exceptional stability, with PCEs recovering to 105% of their initial values after 1000 hours of storage in an Ar atmosphere and retaining 96% of initial efficiency after 1 hour of exposure to ambient air with 80–90% relative humidity. Overall, this study introduces a robust 2D perovskite-like ligand with broad applicability for surface engineering of PbS CQDs, which could be extended to other quantum dots and nanomaterials.

Author contributions

K. L. conducted the experiments and wrote the original manuscript under the supervision of Z. L. Y. Y. and X. Z. helped in the project design and the manuscript writing. B. D. performed solar cell fabrication and measurements and K. L. carried out characterization during revision under the supervision of L. H. D. C. provided the analysis of materials characterization. Z. L. and L. H. led the project. All authors discussed the results and commented on the manuscript.

Conflicts of interest

The authors declare no competing financial interest.

Data availability

The data supporting thsi article have been included as a part of supplementary information (SI). Supplementary information: experimental section and Fig. S1–S7. See DOI: **https://doi.org/10.1039/d5el00135h**.

Acknowledgements

This work was financially supported by the Shanghai Leading Talent Program of Eastern Talent Plan. The authors would like to thank BL03HB beamlines at the Shanghai Synchrotron Radiation Facility (SSRF) for the GIWAXS beamtimes. The authors would also like to thank SCI-GO (**https://www.sci-go.com**) for the FTIR testing. L. Hu acknowledges the Australia Research Council (DE230101711). Z. Liang thanks Prof. X. Gong at the University of Michigan for valuable discussion and comments.

References

1 S. A. McDonald, G. Konstantatos, S. Zhang, P. W. Cyr, E. J. D. Klem, L. Levina and E. H. Sargent, Solution-Processed PbS Quantum Dot Infrared Photodetectors and Photovoltaics, *Nat. Mater.*, 2005, **4**, 138–142.

2 J. M. Luther, M. Law, M. C. Beard, Q. Song, M. O. Reese, R. J. Ellingson and A. J. Nozik, Schottky Solar Cells Based on Colloidal Nanocrystal Films, *Nano Lett.*, 2008, **8**, 3488–3492.

3 C. R. Kagan, E. Lifshitz, E. H. Sargent and D. V. Talapin, Building Devices from Colloidal Quantum Dots, *Science*, 2016, **353**, 885.

4 M. Wu, D. N. Congreve, M. W. B. Wilson, J. Jean, N. Geva, M. Welborn, T. Van Voorhis, V. Bulović, M. G. Bawendi and M. A. Baldo, Solid-State Infrared-to-Visible

Upconversion Sensitized by Colloidal Nanocrystals, *Nat. Photon.*, 2015, **10**, 31–34.

5 R. Saran and R. J. Curry, Lead Sulphide Nanocrystal Photodetector Technologies, *Nat. Photon.*, 2016, **10**, 81–92.

6 R. Azmi, G. Seo, T. K. Ahn and S. Y. Jang, High-Efficiency Air-Stable Colloidal Quantum Dot Solar Cells Based on a Potassium-Doped ZnO Electron-Accepting Layer, *ACS Mater. Interfaces*, 2018, **10**, 35244–35249.

7 M. A. Hines and G. D. Scholes, Colloidal PbS Nanocrystals with Size-Tunable Near-Infrared Emission: Observation of Post-Synthesis Self-Narrowing of the Particle Size Distribution, *Adv. Mater.*, 2003, **15**, 1844–1849.

8 V. Sukhovatkin, S. Hinds, L. Brzozowski and E. H. Sargent, Colloidal Quantum-Dot Photodetectors Exploiting Multiexciton Generation, *Science*, 2009, **324**, 1542–1544.

9 M. L. Böhm, T. C. Jellicoe, M. Tabachnyk, N. J. L. K. Davis, F. Wisnivesky-Rocca-Rivarola, C. Ducati, B. Ehrler, A. A. Bakulin and N. C. Greenham, Lead Telluride Quantum Dot Solar Cells Displaying External Quantum Efficiencies Exceeding 120%, *Nano Lett.*, 2015, **15**, 7987–7993.

10 N. J. L. K. Davis, M. L. Böhm, M. Tabachnyk, F. Wisnivesky-RoccaRivarola, T. C. Jellicoe, C. Ducati, B. Ehrler and N. C. Greenham, Multiple-Exciton Generation in Lead Selenide Nanorod Solar Cells with External Quantum Efficiencies Exceeding 120%, *Nat. Commun.*, 2015, **6**, 8259.

11 Y. Yan, R. W. Crisp, J. Gu, B. D. Chernomordik, G. F. Pach, A. R. Marshall, J. A. Turner and M. C. Beard, Multiple Exciton Generation for Photoelectrochemical Hydrogen Evolution Reactions with Quantum Yields Exceeding 100%, *Nat. Energy*, 2017, **2**, 17052.

12 Y. Liu, H. Wu, G. Shi, Y. Li, Y. Gao, S. Fang, H. Tang, W. Chen, T. Ma, I. Khan, K. Wang, C. Wang, X. Li, Q. Shen, Z. Liu and W. Ma, Merging Passivation in Synthesis Enabling the Lowest Open-Circuit Voltage Loss for PbS Quantum Dot Solar Cells, *Adv. Mater.*, 2022, **35**, 2207293.

13 C. Wang, Y. Wang, Y. Jia, H. Wang, X. Li, S. Liu, X. Liu, H. Zhu, H. Wang, Y. Liu and X. Zhang, Precursor Chemistry Enables the Surface Ligand Control of PbS Quantum Dots for Efficient Photovoltaics, *Adv. Sci.*, 2022, **10**, 2204655.

14 R. Wang, Y. Shang, P. Kanjanaboos, W. Zhou, Z. Ning and E. H. Sargent, Colloidal Quantum Dot Ligand Engineering for High Performance Solar Cells, *Energy Environ. Sci.*, 2016, **9**, 1130–1143.

15 C. Ding, F. Liu, Y. Zhang, S. Hayase, T. Masuda, R. Wang, Y. Zhou, Y. Yao, Z. Zou and Q. Shen, Passivation Strategy of Reducing Both Electron and Hole Trap States for Achieving High-Efficiency PbS Quantum-Dot Solar Cells with Power Conversion Efficiency over 12%, *ACS Energy Lett.*, 2020, **5**, 3224–3236.

16 L. Hu, T. Wan, X. Guan, Z. Li, T. Mei, B. Dong, L. Gao, C. Chen, X. Li, C. H. Lin, M. Li, F. Chen, D. Su, Z. Han, H. Xu, S. Huang, S. Peng, T. Wu and D. Chu, High Performance PbS Colloidal Quantum Dot Solar Cells by Employing Solution-Processed CdS Thin Films from a Single-Source Precursor as the Electron Transport Layer, *Adv. Funct. Mater.*, 2024, **35**, 2419316.

17 M. J. Choi, J. Oh, J. K. Yoo, J. Choi, D. M. Sim and Y. S. Jung, Tailoring of the PbS/Metal Interface in Colloidal Quantum Dot Solar Cells for Improvements of Performance and Air Stability, *Energy Environ. Sci.*, 2014, **7**, 3052–3060.

18 M. J. Choi, F. P. G. de Arquer, A. H. Proppe, A. Seifitokaldani, J. Choi, J. Kim, S. W. Baek, M. Liu, B. Sun, M. Biondi, B. Scheffel, G. Walters, D. Nam, J. W. Jo, O. Ouellette, O. Voznyy, S. Hoogland, S. O. Kelley, Y. S. Jung and E. H. Sargent, Cascade surface modification of colloidal quantum dot inks enables efficient bulk homojunction photovoltaics, *Nat. Commun.*, 2020, **11**, 103.

19 L. Hu, R. J. Patterson, Y. Hu, W. Chen, Z. Zhang, L. Yuan, Z. Chen, G. J. Conibeer, G. Wang and S. Huang, High Performance PbS Colloidal Quantum Dot Solar Cells by Employing Solution-Processed CdS Thin Films from a Single-Source Precursor as the Electron Transport Layer, *Adv. Funct. Mater.*, 2017, **27**, 1703687.

20 C. Ding, D. Wang, D. Liu, H. Li, Y. Li, S. Hayase, T. Sogabe, T. Masuda, Y. Zhou, Y. Yao, Z. Zou, R. Wang and Q. Shen, Over 15% Efficiency PbS Quantum-Dot Solar Cells by Synergistic Effects of Three Interface Engineering: Reducing Nonradiative Recombination and Balancing Charge Carrier Extraction, *Adv. Energy Mater.*, 2022, **12**, 2201676.

21 H. Wang, Z. Zhang, J. Yu, P. C. Lin, C. C. Chueh, X. Liu, S. Guang, S. Qu and W. Tang, Over 15% Efficiency in Ternary Organic Solar Cells by Enhanced Charge Transport and Reduced Energy Loss, *ACS Appl. Mater. Interfaces*, 2020, **12**, 21633–21640.

22 F. Sahli, J. Werner, B. A. Kamino, M. Bräuninger, R. Monnard, B. Paviet-Salomon, L. Barraud, L. Ding, J. J. Diaz Leon, D. Sacchetto, G. Cattaneo, M. Despeisse, M. Boccard, S. Nicolay, Q. Jeangros, B. Niesen and C. Ballif, Fully Textured Monolithic Perovskite/Silicon Tandem Solar Cells with 25.2% Power Conversion Efficiency, *Nat. Mater.*, 2018, **17**, 820–826.

23 J. Kim, J. Jeong, H. Lu, T. K. Lee, F. T. Eickemeyer, Y. Liu, I. W. Choi, S. J. Choi, Y. Jo, H. B. Kim, S. I. Mo, Y. K. Kim, H. Lee, N. G. An, S. Cho, W. R. Tress, S. M. Zakeeruddin, A. Hagfeldt, J. Y. Kim, M. Gratzel and D. S. Kim, Conformal Quantum Dot–SnO_2 Layers as Electron Transporters for Efficient Perovskite Solar Cells, *Science*, 2022, **375**, 302–306.

24 M. Chen, J. Wang, F. Yin, Z. Du, L. A. Belfiore and J. Tang, Strategically Integrating Quantum Dots into Organic and Perovskite Solar Cells, *J. Mater. Chem. A*, 2021, **9**, 4505–4527.

25 G. Seo, J. Seo, S. Ryu, W. Yin, T. K. Ahn and S. I. Seok, Enhancing the Performance of Sensitized Solar Cells with PbS/$CH_3NH_3PbI_3$ Core/Shell Quantum Dots, *J. Phys. Chem. Lett.*, 2014, **5**, 2015–2020.

26 L. Etgar, P. Gao, P. Qin, M. Graetzel and M. K. Nazeeruddin, A Hybrid Lead Iodide Perovskite and Lead Sulfide QD Heterojunction Solar Cell to Obtain a Panchromatic Response, *J. Mater. Chem. A*, 2014, **2**, 11586–11590.

27 Z. Ning, X. Gong, R. Comin, G. Walters, F. Fan, O. Voznyy, E. Yassitepe, A. Buin, S. Hoogland and E. H. Sargent, Quantum-Dot-in-Perovskite Solids, *Nature*, 2015, **523**, 324–328.

28 Z. Yang, A. Janmohamed, X. Lan, F. P. G. de Arquer, O. Voznyy, E. Yassitepe, G. H. Kim, Z. Ning, X. Gong, R. Comin and E. H. Sargent, Colloidal Quantum Dot Photovoltaics Enhanced by Perovskite Shelling, *Nano Lett.*, 2015, **15**, 7539–7543.

29 J. Peng, Y. Chen, X. Zhang, A. Dong and Z. Liang, Solid-State Ligand-Exchange Fabrication of $CH_3NH_3PbI_3$ Capped PbS Quantum Dot Solar Cells, *Adv. Sci.*, 2016, **3**, 1500432.

30 L. Hu, Q. Lei, X. Guan, R. Patterson, J. Yuan, C. H. Lin, J. Kim, X. Geng, A. Younis, X. Wu, X. Liu, T. Wan, D. Chu, T. Wu and S. Huang, Optimizing Surface Chemistry of PbS Colloidal Quantum Dot for Highly Efficient and Stable Solar Cells *via* Chemical Binding, *Adv. Sci.*, 2021, **8**, 2003138.

31 Z. Yang, J. Z. Fan, A. H. Proppe, F. P. G. de Arquer, D. Rossouw, O. Voznyy, X. Lan, M. Liu, G. Walters, R. Q. Bermudez, B. Sun, S. Hoogland, G. A. Botton, S. O. Kelley and E. H. Sargent, Mixed-Quantum-Dot Solar Cells, *Nat. Commun.*, 2017, **8**, 1325.

32 X. Zhang, J. Zhang, D. Phuyal, J. Du, L. Tian, V. A. Öberg, M. B. Johansson, U. B. Cappel, O. Karis, J. Liu, H. Rensmo, G. Boschloo and E. M. J. Johansson, Inorganic $CsPbI_3$ Perovskite Coating on PbS Quantum Dot for Highly Efficient and Stable Infrared Light Converting Solar Cells, *Adv. Energy Mater.*, 2018, **8**, 1702049.

33 M. Liu, Y. Chen, C. S. Tan, R. Q. Bermudez, A. H. Proppe, R. Munir, H. Tan, O. Voznyy, B. Scheffel, G. Walters, A. P. T. Kam, B. Sun, M. J. Choi, S. Hoogland, A. Amassian, S. O. Kelley, F. P. G. de Arquer and E. H. Sargent, Lattice Anchoring Stabilizes Solution-Processed Semiconductors, *Nature*, 2019, **570**, 96–101.

34 M. A. Siguan, D. B. Koch, A. D. Taylor, Q. Sun, V. L. G. Ippenheimer, F. Paulus and Y. Vaynzof, Efficient and Stable PbS Quantum Dot Solar Cells by Triple-Cation Perovskite Passivation, *ACS Nano*, 2020, **14**, 384–393.

35 B. Sun, A. Johnston, C. Xu, M. Wei, Z. Huang, Z. Jiang, H. Zhou, Y. Gao, Y. Dong, O. Ouellette, X. Zheng, J. Liu, M. J. Choi, Y. Gao, S. W. Baek, F. Laquai, O. M. Bakr, D. Ban, O. Voznyy, F. P. G. de Arquer and E. H. Sargent, Monolayer Perovskite Bridges Enable Strong Quantum Dot Coupling for Efficient Solar Cells, *Joule*, 2020, **4**, 1542–1546.

36 J. Yang, S. C. Cho, S. Lee, J. W. Yoon, W. H. Jeong, H. Song, J. T. Oh, S. G. Lim, S. Y. Bae, B. R. Lee, M. Ahmadi, E. H. Sargent, W. Yi, S. U. Lee and H. Choi, Guanidinium-Pseudohalide Perovskite Interfaces Enable Surface Reconstruction of Colloidal Quantum Dots for Efficient and Stable Photovoltaics, *ACS Nano*, 2022, **16**, 1649–1660.

37 X. Zhang, G. Wu, W. Fu, M. Qin, W. Yang, J. Yan, Z. Zhang, X. Lu and H. Chen, Orientation Regulation of Phenylethylammonium Cation Based 2D Perovskite Solar Cell with Efficiency Higher Than 11%, *Adv. Energy Mater.*, 2018, **8**, 1702498.

38 J. Xu, O. Voznyy, M. Liu, A. R. Kirmani, G. Walters, R. Munir, M. Abdelsamie, A. H. Proppe, A. Sarkar, F. P. G. de Arquer, M. Wei, B. Jun, M. Liu, O. Ouellette, R. Q. Bermudez, J. Li, J. Fan, L. Quan, P. Todorovic, H. Tan, S. Hoogland, S. O. Kelley, M. Stefik, A. Amassian and E. H. Sargent, 2D Matrix Engineering for Homogeneous Quantum Dot Coupling in Photovoltaic Solids, *Nat. Nanotech.*, 2018, **13**, 456–462.

39 M. A. Siguan, D. B. Koch, E. C. Baird, Y. J. Hofstetter, B. P. Carwithen, A. Kirch, S. Reineke, A. A. Bakulin, F. Paulus and Y. Vaynzof, Interdot Lead Halide Excess Management in PbS Quantum Dot Solar Cells, *Adv. Energy Mater.*, 2022, **12**, 2202994.

40 L. Gao, L. N. Quan, F. P. G. de Arquer, Y. Zhao, R. Munir, A. Proppe, R. Q. Bermudez, C. Zou, Z. Yang, M. I. Saidaminov, O. Voznyy, S. Kinge, Z. Lu, S. O. Kelley, A. Amassian, J. Tang and E. H. Sargent, Efficient Near-Infrared Light-Emitting Diodes Based on Quantum Dots in Layered Perovskite, *Nat. Photon.*, 2020, **14**, 227–233.

41 W. Pan, M. Tan, Y. He, H. Wei and B. Yang, Organic Amine-Bridged Quasi-2D Perovskite/PbS Colloidal Quantum Dots Composites for High-Gain Near-Infrared Photodetectors, *Nano Lett.*, 2022, **6**, 2277–2284.

42 Y. Wang, K. Singh, J. Li, Y. Dong, X. Wang, J. M. Pina, Y. Yu, R. Sabatini, Y. Liu, D. Ma, J. Liu, Z. Liu, Y. Gao, O. Voznyy, W. Ma, M. Fung, L. Liao and E. H. Sargent, In Situ Inorganic Ligand Replenishment Enables Bandgap Stability in Mixed-Halide Perovskite Quantum Dot Solids, *Adv. Mater.*, 2022, **34**, 2200854.

43 R. Wu, Y. Yang, M. Li, D. Qin, Y. Zhang and L. Hou, Solvent Engineering for High-Performance PbS Quantum Dots Solar Cells, *Nanomaterials*, 2017, **7**, 201.

44 G. Shi, H. Wang, Y. Zhang, C. Cheng, T. Zhai, B. Chen, X. Liu, R. Jono, X. Mao, Y. Liu, X. Zhang, X. Ling, Y. Zhang, X. Meng, Y. Chen, S. Duhm, L. Zhang, T. Li, L. Wang, S. Xiong, T. Sagawa, T. Kubo, H. Segawa, Q. Shen, Z. Liu and W. Ma, The effect of Water on Colloidal Quantum Dot Solar Cells, *Nat. Commun.*, 2021, **12**, 4381.

45 L. Gao, L. N. Quan, F. P. García de Arquer, Y. Zhao, R. Munir, A. Proppe, R. Quintero-Bermudez, C. Zou, Z. Yang, M. I. Saidaminov, O. Voznyy, S. Kinge, Z. Lu, S. O. Kelley, A. Amassian, J. Tang and E. H. Sargent, Efficient Near-Infrared Light-Emitting Diodes based on Quantum Dots in Layered Perovskite, *Nat. Photonics*, 2020, **14**, 227–233.

46 M. Liu, O. Voznyy, R. Sabatini, F. P. García de Arquer, R. Munir, A. H. Balawi, X. Lan, F. Fan, G. Walters, A. R. Kirmani, S. Hoogland, F. Laquai, A. Amassian and E. H. Sargent, Hybrid Organic–Inorganic Inks Flatten the Energy Landscape in Colloidal Quantum Dot Solids, *Nat. Mater.*, 2016, **16**, 258–263.

47 Z. Ning, X. Gong, R. Comin, G. Walters, F. Fan, O. Voznyy, E. Yassitepe, A. Buin, S. Hoogland and E. H. Sargent, Quantum-Dot-in-Perovskite Solids, *Nature*, 2015, **523**, 324.

48 I. Moreels, K. Lambert, D. Smeets, D. D. Muynck, T. Nollet, J. C. Martins, F. Vanhaecke, A. Vantomme, C. Delerue, G. Allan and Z. Hens, Size-Dependent Optical Properties of Colloidal PbS Quantum Dots, *ACS Nano*, 2009, **3**, 3023–3030.

49 T. Liu, B. Xiao, F. Xiang, J. Tan, Z. Chen, X. Zhang, C. Wu, Z. Mao, G. Luo, X. Chen and J. Deng, Ultrasmall Copper-

Based Nanoparticles for Reactive Oxygen Species Scavenging and Alleviation of Inflammation Related Diseases, *Nat. Commun.*, 2020, **11**, 2788.

50 L. Hu, D. B. Li, L. Gao, H. Tan, C. Chen, K. Li, M. Li, J. B. Han, H. Song, H. Liu and J. Tang, Graphene Doping Improved Device Performance of ZnMgO/PbS Colloidal Quantum Dot Photovoltaics, *Adv. Funct. Mater.*, 2016, **26**, 1899–1907.

51 S. Liu, L. Hu, S. Huang, W. Zhang, J. Ma, J. Wang, X. Guan, C. H. Lin, J. Kim, T. Wan, Q. Lei, D. Chu and T. Wu, Enhancing the Efficiency and Stability of PbS Quantum Dot Solar Cells through Engineering an Ultrathin NiO Nanocrystalline Interlayer, *ACS Appl. Mater. Interfaces*, 2020, **12**, 46239–46246.

52 Y. Xia, S. Liu, K. Wang, X. Yang, L. Lian, Z. Zhang, J. He, G. Liang, S. Wang, M. Tan, H. Song, D. Zhang, J. Gao, J. Tang, M. C. Beard and J. Zhang, Cation-Exchange Synthesis of Highly Monodisperse PbS Quantum Dots from ZnS Nanorods for Efficient Infrared Solar Cells, *Adv. Funct. Mater.*, 2019, **30**, 1907379.